CHEMISTRY OF MATERIALS

Open Access

pubs.acs.org/cm

Article

Alternative Polymorph of the Hydroxysulfate Li_xFeSO_4OH Yields Improved Lithium-Ion Cathodes

Shashwat Singh, Arup Chakraborty, Audric Neveu, Pawan Kumar Jha, Valérie Pralong, Maximilian Fichtner, M. Saiful Islam,* and Prabeer Barpanda*

Cite This: *Chem. Mater.* 2024, 36, 8088–8097

Read Online

ACCESS | Metrics & More | Article Recommendations | Supporting Information

ABSTRACT: Use of sustainable electrode components in Li-ion battery technology is essential for large-scale applications while addressing environmental concerns. Considering elemental abundance, Fe-based compounds can, in principle, work as the most economic cathodes. Fe-based hydroxysulfates Li_xFeSO_4OH (x = 0 −1) can be harnessed as low-cost, sustainable, high-voltage, and moisture-resistant battery cathode materials. In this system, monoclinic (m) $FeSO_4OH$ and layered m-$FeSO_4OH$ were previously reported as Li-ion battery cathode materials. Here, we introduce orthorhombic (o) $FeSO_4OH$ as a potential low-cost cathode for Li-ion batteries synthesized by using a facile low-temperature hydrothermal route. The o-$FeSO_4OH$ cathode delivers a reversible capacity of 100 mA h/g at a current rate of C/20 ($1e^- = 159$ mAh/g) at a working potential of ca. 3.2 V vs Li^+/Li. A higher overpotential and faster rate kinetics compared with that of m-$FeSO_4OH$ stem from the subtle deviations in the structural framework affecting the Li coordination environment. Operando analytical tools, electrochemical titration techniques, and computational modeling are combined to characterize the complex phase transformation during the (de)lithiation process.

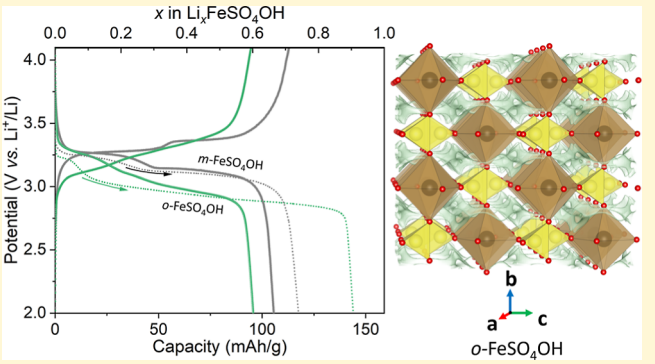

1. INTRODUCTION

Lithium-ion battery technology has ushered in the wide-scale use of portable consumer electronic devices and has now brought us to the cusp of the electric vehicle revolution. The factors related to the operation of cathodes, such as high energy density, low-cost, environmental issues, and sustainability, are crucial to the large-scale deployment of Li-ion batteries.[1,2] Although the layered oxide-based cathode materials satisfy the high energy density requirement,[3] they suffer from the high cost of Ni and Co metals. From a transition metal perspective, Fe-based materials form the most economic cathodes, with Fe being the most abundant 3d transition metal and the fourth most abundant element in the Earth's crust.[4] Unfortunately, Fe-based layered oxides are structurally unstable and ineffective for Li^+ (de)intercalation, which has led to the exploration of polyanionic materials as cathode hosts having earth-abundant constituent elements and ease of synthesis.

The electronegative polyanionic units (X) in polyanionic materials activate the inductive effect by increasing the ionicity of the metal (M)−oxygen (O) bond in the M−O−X framework, thereby resulting in decreased separation between the bonding and antibonding orbitals.[5] The ripple effect of this phenomenon is observed in the increased redox potential of the M^{3+}/M^{2+} redox couple. For a competitive energy density, the position of the redox couple can be tuned strategically to offset the theoretical capacity loss due to the mass of the polyanionic units. This pursuit has unveiled suites of polyanion-type cathode materials, including $LiFePO_4$, Li_2FeSiO_4, and $Li_2FeP_2O_7$.[6−9] Exploiting the highly electronegative sulfate moieties, the fluorosulfates $AMSO_4F$ (A = Li, Na, and K; M = 3d metals) have set the benchmark of the highest potential of the Fe^{3+}/Fe^{2+} redox couple as seen in triplite $LiFe^{II}SO_4F$ (3.9 V vs Li^+/Li).[10] This marked an enhancement of 300 mV over the redox potential of Fe^{3+}/Fe^{2+} at 3.6 V reported for the tavorite polymorph of $LiFe^{II}SO_4F$,[11] as a result of edge-shared FeO_4F_2 octahedra.[12] However, these fluorosulfates are air-sensitive, demanding special material processing and careful handling protocols.[13] Furthermore, they contain environmentally hazardous fluorine, rendering them unsuitable for large-scale electrode applications.

In pursuit of fluorine-free and moisture-resistant analogues of the $LiFeSO_4F$ material, hydroxy-based polyanionic materials

Received: June 12, 2024
Revised: July 24, 2024
Accepted: July 25, 2024
Published: August 15, 2024

can offer alternatives.[14] Indeed, Pralong et al. reported monoclinic (m)-$Fe^{III}SO_4OH$ (s.g. $C2/c$) having Fe^{3+}/Fe^{2+} redox couple centered at 3.2 V (vs Li^+/Li) following a two-step biphasic reaction mechanism.[15−17] Noteworthy is the decrease in the redox potential by 400 mV compared to tavorite $LiFeSO_4F$ stemming from the reduced inductive effect of the OH^- vis-à-vis F^- moiety. Interestingly, for $FeSO_4F_{1-y}OH_y$ ($0.35 < y < 1$) phases, the Li (de)insertion mechanism was dependent on samples with F^- content.[18] To overcome the voltage penalty, layered m-$LiFe^{II}SO_4OH$ (s.g. $P2_1/c$) having edge-shared $Fe(OH)_2O_4$ octahedra was reported working as a 3.6 V (vs Li^+/Li) cathode material based on the single-phase topotactic insertion mechanism. However, the interlayer van der Waals interaction hindered fast Li^+ migration resulting in moderate rate capability in comparison to tavorite $LiFe^{II}SO_4OH$.[19] This offers room to discover new Fe-based cathodes that combine low materials cost, ease of synthesis, and efficient electrochemical activity.

By exploiting polymorphism in polyanionic frameworks, here we have introduced an orthorhombic (o) polymorph of the $Fe^{III}SO_4OH$ hydroxysulfate compound (referred to as *o*-FSH from now onward) as a novel Li-ion insertion material. A suite of electrochemical techniques has been combined with first-principles calculations based on density functional theory (DFT) to gain mechanistic insights into the electrochemical properties. The *o*-FSH compound offers the advantage of ease of synthesis based on a low-temperature hydrothermal synthesis route using an earth-abundant sustainable precursor. With excellent moisture resistance, it can work as a low-cost, robust 3.2 V cathode for Li-ion batteries.

2. RESULTS AND DISCUSSION

2.1. Crystal Structure and Morphology. The polyanionic sulfate compounds are known to offer rich crystal chemistry and polymorphism, which, in turn, affect the redox mechanism and electrochemical properties. For instance, monoclinic and rhombohedral polymorphs of $Fe_3(SO_4)_2$ follow a biphasic and solid solution reaction mechanism during Li (de)insertion, respectively.[20] Similarly, tavorite $FeSO_4OH$ and layered $LiFeSO_4OH$ exhibit biphasic and solid solution mechanisms, respectively, to store Li.[18,21] Furthermore, polymorphic changes can enhance the redox potential for the same composition (3.6 V for tavorite $LiFeSO_4F$ vs. 3.9 V triplite $LiFeSO_4F$).[10,11]

In this light, an orthorhombic polymorph of $FeSO_4OH$ (*o*-FSH) was synthesized using a facile low-temperature hydrothermal synthesis route at 190 °C for 5 h using a commercially available low-cost $Fe_2(SO_4)_3{\cdot}xH_2O$ precursor.[22] In comparison, synthesis of previously reported monoclinic (m) $FeSO_4OH$ was cumbersome, involving higher annealing temperature and longer duration (ca. 280 °C—1 week). The phase purity of as-prepared *o*-FSH was confirmed by Rietveld analysis of the high-resolution XRD pattern, using ICSD: 24079 (s.g. *Pnma*)[22] as the reference model, as shown in Figure 1a. The corresponding crystallographic parameters are presented in Table S1 (Supporting Information). When compared to the monoclinic $FeSO_4OH$ (*m*-FSH) and layered $LiFeSO_4OH$ (*lay*-LiFSH) polymorphs as well as the bisulfate and fluorosulfate cathode compounds, *o*-FSH offers several advantages with respect to the ease of synthesis, low-cost precursor, and ambient moisture resistance.

The effect of variation in synthesis conditions, such as the annealing temperature and time, on the product phase and

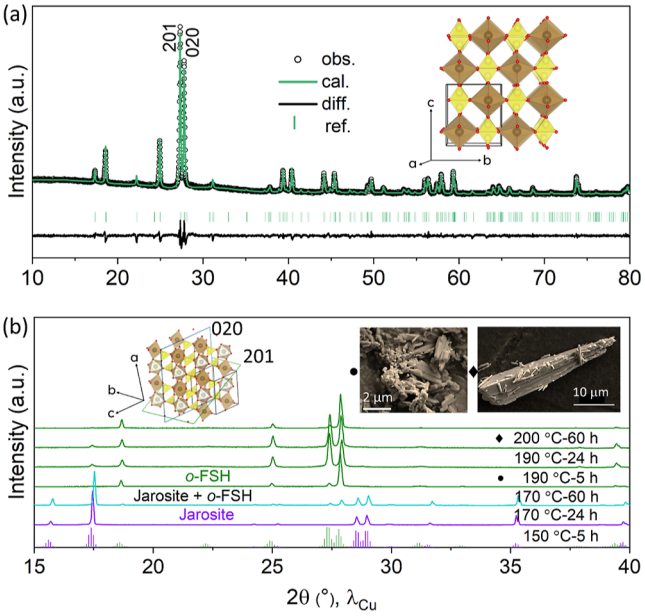

Figure 1. (a) Rietveld analysis of *o*-FSH (s.g. *Pnma*) performed on the high-resolution XRD pattern. obs., observed; cal., calculated; diff., difference; ref., reference. Inset: Crystal structure of *o*-FSH along the *a*-axis. Yellow, brown, and red color represent sulfur (tetrahedra), iron (octahedra), and oxygen atoms, respectively. (b) Comparative XRD patterns of products obtained from variations in the hydrothermal synthesis conditions with respect to temperature and time. Inset (left). (020) and (201) planes shown for *o*-FSH projected along a hexagonal tunnel. (Right) Rod-like morphology of the pristine material synthesized at 190 °C—5 h and 200 °C—60 h. Note the preferred growth of the (020) plane.

morphology is shown in Figure 1b. At a lower temperature and time of synthesis (ca. 150 °C−5 h), the hydronium jarosite $(H_3O)Fe_3(OH)_6(SO_4)_2$ phase was formed.[23,24] In addition, synthesis at 200 °C−60 h resulted in the formation of *o*-FSH with preferential growth along the (020) plane, which was also found to be the lowest energy surface plane from the surface energy calculations, as discussed later. This observation was further confirmed by its rod-like morphology exposing the (020) plane (Figure 1b inset). In the intermediate region at 170 °C−24 h, a mixture of the hydronium jarosite and o-FSH phases was observed. The formation of the *o*-FSH phase evidently occurs at the expense of the hydronium jarosite.

The structure of *o*-FSH is shown in Figure 1a inset, which is composed of $[FeOHSO_4]^2$ chains formed by $FeO_4(OH)_2$ octahedra linked to SO_4 tetrahedra along the equatorial plane. A 3D framework is formed as the apical oxygens connected with hydrogen shared with other Fe-octahedra. The chains are stacked along the *b*-axis. It is noted that the crystal framework of *m*-FSH (s.g. $C2/c$) can be obtained by moving the upper layer of *o*-FSH by a/2 with respect to the layer immediately below it.[25] This *o*-FSH framework offers ample room to accommodate Li-ion insertion in the vacant spaces along the *a*-axis.

A comparison of XRD patterns of $FeSO_4OH$ polymorphs is shown in Figure S1 in Supporting Information. A close inspection of the two polymorphs of *o*-FSH (Figure 2a−c) and *m*-FSH (Figure 2d−f) reveals very tiny structural variations. Although, in both cases, the iron octahedra share corners with four SO_4 tetrahedra and two $FeO_4(OH)_2$ octahedra moieties, one of the SO_4 tetrahedra (encircled) is oriented differently in

https://doi.org/10.1021/acs.chemmater.4c01652
Chem. Mater. 2024, 36, 8088−8097

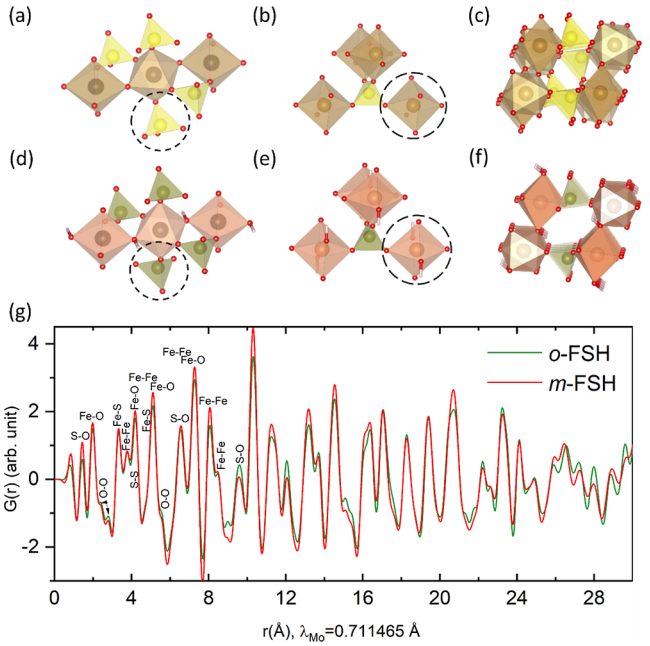

Figure 2. Comparative illustration of local structural variations between *o*-FSH (a–c) and *m*-FSH (d–f) based on structural information obtained from powder diffraction. (a,d) Sulfate tetrahedra, (b,e) iron octahedra and (c,f) hexagonal tunnel. (g) Comparative PDF analysis of *o*-FSH (green line) and *m*-FSH (red line) polymorphs was performed on total scattering data affirming minute local structural variations.

o-FSH. Similarly, one of the iron octahedra connected to SO_4 tetrahedra in *o*-FSH can be obtained by a clockwise rotation from the corresponding arrangement in *m*-FSH. As a result, the hexagonal tunnel encompassed by the $FeO_4(OH)_2$ and SO_4 moieties is partially blocked by alternating SO_4 tetrahedra in *o*-FSH vis-à-vis *m*-FSH.

The exact orientation of the O–H bonds, not shown in *o*-FSH (Figure 2a–c), remains to be established from neutron powder diffraction (NPD) and DFT calculations. The O–H bond would likely be aligned parallel to the equatorial plane of iron octahedra connected to four sulfate tetrahedra and two iron octahedra, as in the case of *m*-FSH. The orientational disorder at high temperatures due to the rotational motion of the translationally static sulfate ions has been exhibited by polyanionic sulfates such as Li_2SO_4, $Li_4Zn(SO_4)_3$, etc.[26] While there is no thermal and temporal phase transition between *m*-FSH[27,28] and *o*-FSH (Figure S2 in Supporting Information), the hydrothermal synthesis route used in the study might play a role in disorienting $[SO_4]^{2-}$ polyanions in the *o*-FSH phase. The very small structural differences between these two polymorphs are further substantiated by PDF analysis (Figure 2g) of total scattering data, and both Bragg and diffuse scattering data were obtained from a sample contained in quartz capillary using a high-energy Mo (0.711465 Å) X-ray source. The PDF provides information about the real space distribution of interatomic distances.[29] The PDF patterns of both FSH polymorphs do not completely overlap, with noticeable deviations observed for the distribution of S–O, O–O, Fe–Fe, and Fe–O bond distances. Overall, the frameworks of *o*-FSH and *m*-FSH are largely similar, thus offering similar average redox potentials for the Fe^{3+}/Fe^{2+} redox couple. However, the orientational disorder of sulfate polyanions in the Li migration channels may result in a sloped (dis)charge profile for *o*-FSH as opposed to the flat biphasic (dis)charge profile reported for *m*-FSH.[20,30]

The atomic-scale structural changes during Li (de)insertion in the *o*-FSH structure have been investigated by using combined DFT and force-field-based methods. The calculations started using a fully delithiated structure of *o*-FSH (Figure 1a, Table S1 in Supporting Information), as obtained from Rietveld analysis. The calculated structural parameters were compared to the experimental values obtained from XRD data, as listed in Table 1, revealing a good reproduction of the lattice parameters of *o*-FSH.

Table 1. (a) Structural Parameters of *o*-FSH Calculated with DFT + *U* and Compared with the Experimental Structure. (b) Comparison between Calculated and Experimental Cell Voltage Values (vs Li/Li^+) for *o*-LiFSH

(a)

o-FSH parameters	experimental	calculated	difference (Δ, %)
a (Å)	7.338	7.311	0.37
b (Å)	6.418	6.442	0.37
c (Å)	7.139	7.089	0.71
mean *α*, *β*, *γ* (deg)	90.0	90.2	0.22
volume ($Å^3$)	336.21	333.84	0.71

(b)

x in Li_xFSH	calculated voltage (V)	experimental voltage (V)
1.0 to 0.5	3.34	~3.30
0.5 to 0.0	2.57	~2.90

For the simulations of the unresolved lithiated structure, Li ions were then inserted at the 4a sites in the *o*-FSH structure (Figure 3a) with the *Pnma* space group, and full geometrical

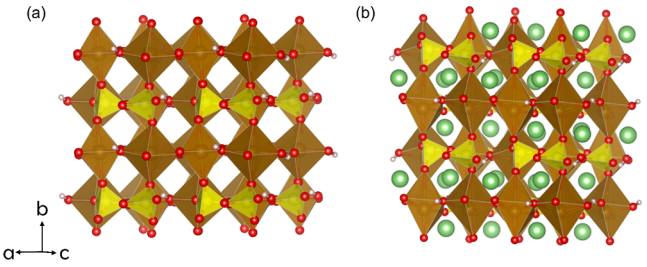

Figure 3. Simulated structures of (a) *o*-FSH and (b) *o*-LiFSH. Here, Li, Fe, S, O, and H atoms are shown in green, brown, yellow, red, and light pink, respectively.

relaxation of the cell volume and coordinates was performed. Using this initial relaxed structure, *ab initio* molecular dynamics (AIMD) simulations were then conducted to find the favorable Li positions within the unit cell at room temperature, and the final optimized structure is shown in Figure 3b. It was found that the Fe octahedra in the *o*-LiFSH structure are more distorted than in *o*-FSH and the Li-ions also have a slightly distorted octahedral environment. This structure of *o*-LiFSH is similar to that of the monoclinic polymorph *m*-LiFSH, where the Li and Fe ions are arranged in alternative layers. Here, the layer structure is along the crystallographic *b*-direction (see Figure 3b).

Previous studies on cathode materials have established DFT methods as valuable tools to probe Li (de)insertion reactions and to predict trends in cell voltage.[35–37] Using the minimized energies of the various relaxed structures corresponding to

https://doi.org/10.1021/acs.chemmater.4c01652
Chem. Mater. 2024, 36, 8088–8097

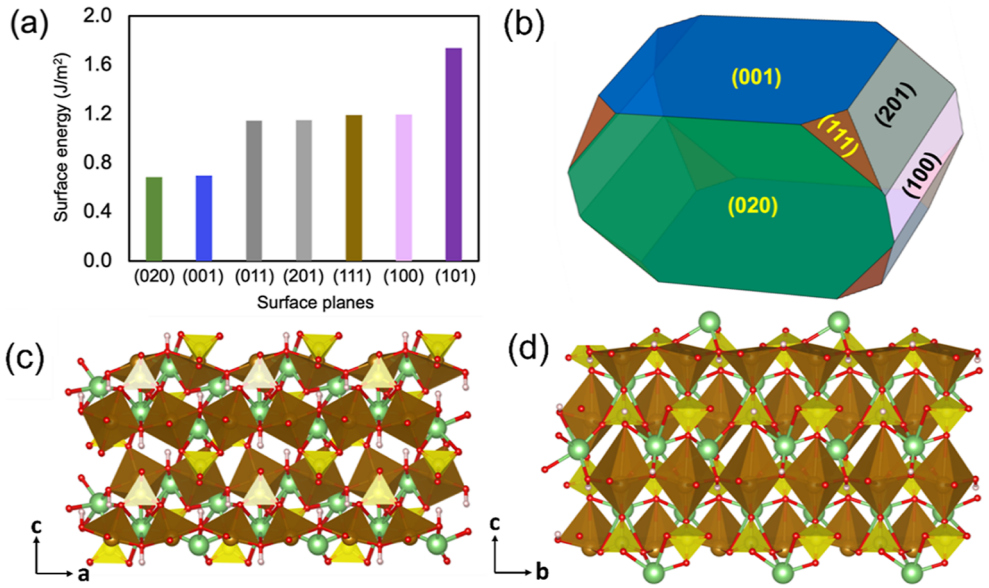

Figure 4. (a) Calculated surface energies for possible surface planes of *o*-LiFSH. (b) Wulff construction[31] of the equilibrium morphology of *o*-LiFSH, composed of (020), (001), (201), (111), and (100) planes. The calculated shape resembles the experimentally observed prolate-like morphology. Side view of (c) (001) and (d) (020) surfaces of o-LiFSH. The green, brown, and yellow colors represent Li ion, FeO_6 octahedra, and SO_4 tetrahedra, respectively.

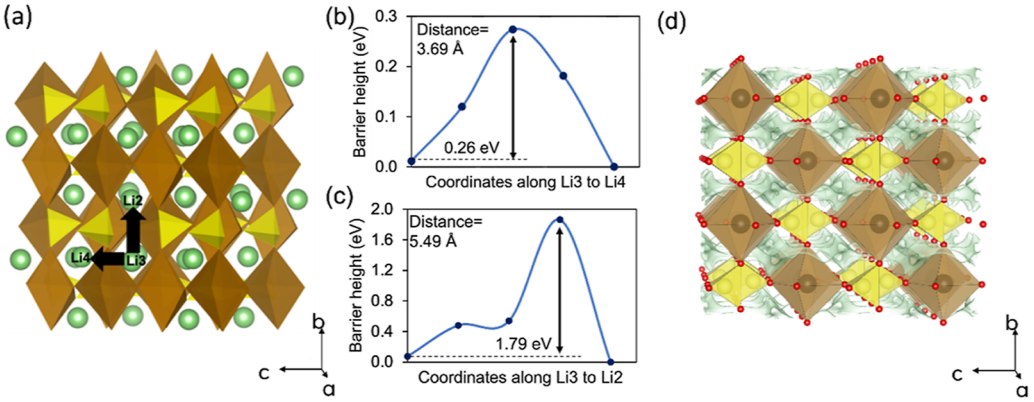

Figure 5. (a) Possible pathways for Li-ion diffusion in *o*-LiFSH. Brown polygons are FeO_6 octahedra and yellow polygons are SO_4 tetrahedra. Activation energy barriers for Li-ion migration from nudged elastic band (NEB) calculations along (b) Li3 to Li4 and (c) Li3 to Li2. (d) Iso-surface landscapes for the 2D Li migration pathway in *o*-FSH along the (010) plane from BVSE calculations. The Li3−Li4 pathway would be preferred, restraining the Li-ion diffusion parallel to the (010) plane via 2D pathways.

Li_xFeSO_4OH ($0 \le x \le 1$), the voltages of Fe^{2+}/Fe^{3+} (vs Li^+/Li^0) were computed [see Computational Methods (Section 4.5)]. The average calculated intercalation voltages for x ranging from 1.0 to 0.5 and 0.5 to 0 are compared with the experimental values listed in Table 1b, which are in close agreement (Δ = 0.04 V for x = 1.0−0.5 and Δ = 0.33 V for x = 0.5−0), indicating the validity of the predicted lithiated structures.

Electrode kinetics can be affected by particle morphology and whether its surfaces expose facile Li ion channels. Therefore, we investigated possible unique surface planes of *o*-LiFSH after reproducing its bulk structure. The surface energies (SEs) obtained from the modeling of crystal facets and their corresponding symmetry-constrained equivalent surfaces are summarized in Figure 4a [and Table S2 (Supporting Information)]. Among the surface facets examined, the (020) and (001) facets have the lowest SEs and are found to dominate the predicted equilibrium prolate-shaped morphology (Figure 4b). The (020) and (001) surfaces, which have interconnected $FeO_4(OH)_2$ and SO_4 polyhedra, are shown in Figure 4c,d, respectively. This equilibrium morphology agrees well with the observed morphology obtained using the hydrothermal synthesis route with significant exposure of the (020) plane (Figure 1b). This finding underscores the role of the synthesis route in influencing particle morphology.

2.2. Intrinsic Defects and Li-Ion Migration Pathways.

Examining point defects is crucial to fully understand the structural and electrochemical behavior of cathode materials. The defect energies in *o*-LiFSH were calculated for a range of defect types with a focus on Li-Frenkel and Li/Fe antisite, which are generally prominent for polyanion cathode materials. These defect reactions are represented by the following equations using Kröger−Vink notation

$$\text{Li Frenkel: } Li_{Li}^{\times} \rightarrow V_{Li}' + Li_i^{\bullet} \quad (1)$$

$$\text{Li/Fe antisite: } Li_{Li}^{\times} + Fe_{Fe}^{\times} \rightarrow Li_{Fe}' + Fe_{Li}^{\bullet} \quad (2)$$

https://doi.org/10.1021/acs.chemmater.4c01652
Chem. Mater. 2024, 36, 8088−8097

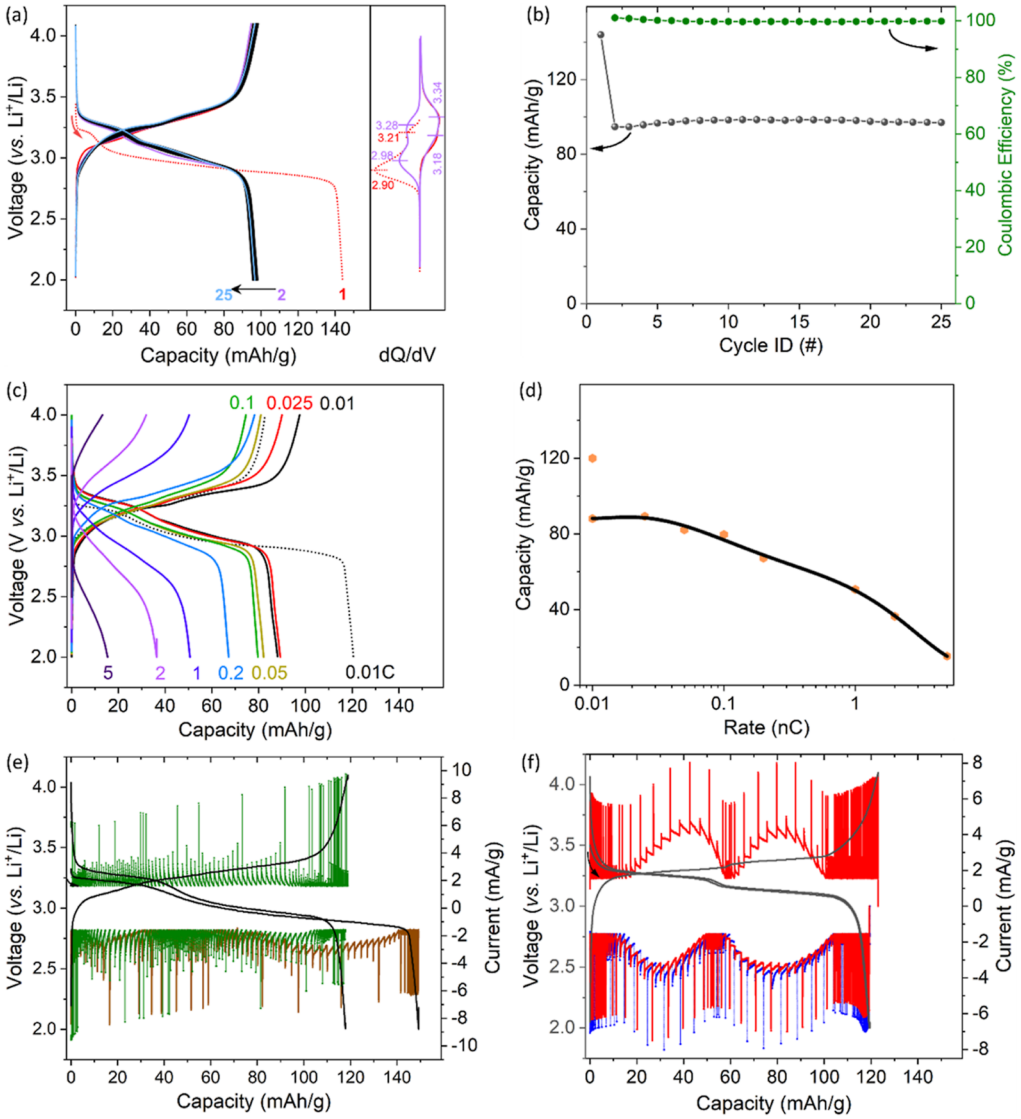

Figure 6. (a) Galvanostatic (dis)charge profile for *o*-FSH, with corresponding differential capacity curve of the first two cycles, acquired at a current rate of C/20 in a Swagelok-type half-cell configuration. 1 M $LiClO_4$ dissolved in PC was used as an electrolyte. (b) The capacity retention was observed over 25 cycles. (c) Galvanostatic profiles for *o*-FSH are shown at different current rates. (d) The discharge capacity as a function of the rate suggests moderate rate kinetics. Potentiostatic intermittent titration technique (PITT) curve for (e) *o*-FSH and (f) *m*-FSH at a potential step of 5 mV for 1 h with current decay set to $|i| \leq C/100$. Note the current decay behavior of *o*-FSH and *m*-FSH. *o*-FSH has a wider solid solution region.

Since Li^+ (radius 0.74 Å) and Fe^{2+} (radius 0.78 Å) ions have a similar radius, they may show antisite defect behaviour, which has been reported for other polyanionic materials such as olivine-structured $LiMPO_4$ (M = Mn, Fe, Co, and Ni).[32,33] The calculations on *o*-LiFSH led to defect energies for the Li-Frenkel of 2.45 eV and Li/Fe antisite defect of 1.15 eV; the antisite value is lower than in tavorite-LiFSH[19] and layered-LiFSH,[18] suggesting possible Li/Fe antisite disorder as found in $LiFePO_4$. It is recognized that electrochemical lithiation of LiFSH may reduce the likelihood of such disorder. This warrants further investigation of *o*-LiFSH on cycling using NPD and Li nuclear magnetic resonance analyses.

Atomistic modeling can provide insights into Li-ion mobility and favorable pathways, which is vital in understanding the rate of charge/discharge of the cathode materials. The migration barriers were calculated along two possible paths for Li-ion diffusion within *o*-LiFSH: (path 1) the Li3 to Li4 hop parallel to the (010) plane having a Li−Li distance of 3.69 Å, and (path 2) Li3 to Li2 hop along the [010] direction or *b*-axis with a Li−Li distance of 5.49 Å (see Figure 5a−c). The calculated activation barriers for Li-ion migration along path 1 and path 2 are 0.26 and 1.79 eV, respectively. Hence, the Li migration will be favored along a 2D pathway parallel to the (010) plane. A qualitatively similar observation is drawn from bond valence site energy (BVSE) analysis,[34] confirming the primarily 2D pathway for Li migration, as shown for *o*-FSH in Figures 5d and S3 (Supporting Information).

2.3. Electrochemical Measurements with Operando and Ex-Situ Analyses. The electrochemical performance of as-synthesized *o*-FSH was evaluated in a half-cell configuration against Li metal foil as a negative electrode using Swagelok-type cells or CR2032 coin-type cells. The galvanostatic (dis)charge profile of the *o*-FSH electrode acquired at a current rate of C/20 ($1e^-$ = 159 mA h/g) is shown in Figure

https://doi.org/10.1021/acs.chemmater.4c01652
Chem. Mater. 2024, 36, 8088−8097

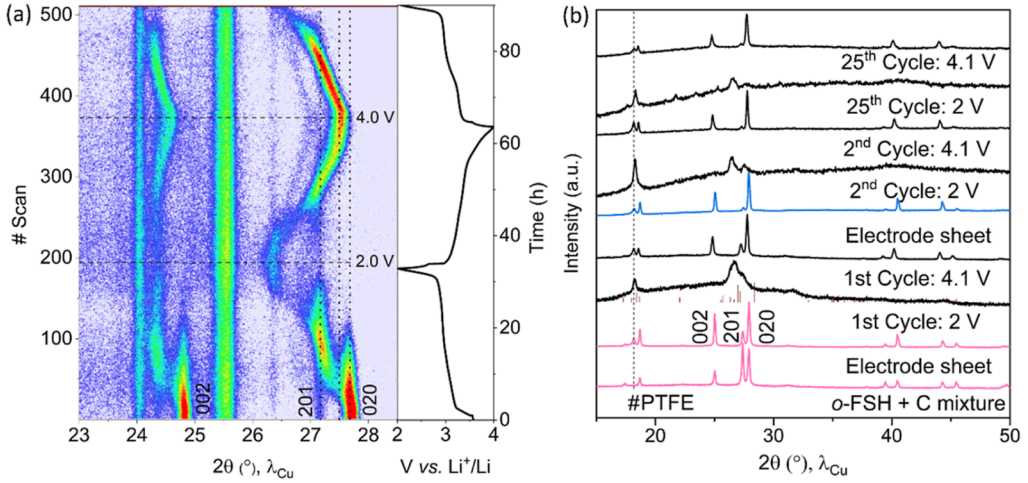

Figure 7. (a) Operando X-ray diffraction patterns recorded during first discharge and subsequent (dis)charge of Li/Li$_x$FSH cell. The plot on the right corresponds to the galvanostatic profile at a current rate of C/35. The states of 2.0 and 4.0 V are marked with dashed lines. (b) Ex-situ X-ray diffraction patterns at 1st, 2nd, and 25th cycles. The XRD pattern for the electrode sheet and *o*-FSH and C mixture corresponds to the pristine state. Note the excellent reversibility after 25 cycles.

6a. The first discharge capacity is ca. 142 mA h/g (0.89 mol Li^+) with two distinct steps implying structural rearrangement: first up to a capacity of 10 mA h/g centered at 3.2 V and the second from 20 to 140 mA h/g centered at 2.9 V. In the subsequent charge, 100 mA h/g (0.63 Li^+) is extracted following a notably sloped profile suggesting a single-phase reaction mechanism. The following (dis)charge cycles retrace the same sloped profile with good capacity retention (ca. 60%) and Coulombic efficiency (ca. 100%) over 25 cycles (Figure 6b). A similar profile was observed even with a very slow rate of Li (de)insertion at C/80 with intermittent equilibration of 1 h, using the galvanostatic intermittent titration technique (GITT), as shown in Figure S4 of Supporting Information. This result suggests that kinetic factors do not dictate the Li reaction mechanism of *o*-FSH. Similar electrochemical behavior was observed for the powder cell at a current rate of C/20 (Figure S5 in Supporting Information).

The rate capability of *o*-FSH was measured at different current rates of C/100 (0.01 C), C/40 (0.025 C), C/20 (0.05 C), C/10 (0.1 C), C/5 (0.2), 1 C, 2 C, and 5 C resulting in discharge capacities of 88, 89, 82, 80, 67, 51, 37, and 15 mA h/g, respectively (see Figure 6c,d). The steep fall in discharge capacities at higher current rates is often observed for polyanionic sulfates and likely stems from their poor electronic conductivity. Nonetheless, the moderate rate kinetics of pristine *o*-FSH is notable, leaving room for further enhancement by employing electrode engineering measures such as nanocarbon coating and intimate milling with conductive carbon.

At this point, the electrochemical activity of *o*-FSH is compared with that of *m*-FSH (see Figure S6 in Supporting Information). *m*-FSH delivers a reversible capacity of 105 mA h/g, after the first discharge capacity of 117 mA h/g, with a redox potential of Fe^{3+}/Fe^{2+} situated at 3.2 V, which accords with the report by Pralong et al.[16] The two-step biphasic redox reaction of *m*-FSH is based on the change in the coordination environment of Li from octahedral to tetrahedral geometry corresponding to up to 50 and 100% Li accommodation within the *m*-FSH framework.[18] The mechanistic deviation of *o*-FSH from *m*-FSH was investigated by using the potentiostatic intermittent titration technique (PITT). The resultant current decay behavior, under the condition of $|i| \leq C/100$ after a potential step of 5 mV for 1 h, superimposed on the voltage vs capacity plot, is shown in Figure 6d,e. Since the excitation lasts 1 h, the capacity on the *x*-axis can also serve as a function of time. Two shallow bell-shaped curves seen during the first discharge of *o*-FSH (brown line) can stem from a non-Cottrellian-type current response, characteristic of a phase change, along the two plateaus. These non-Cottrellian regions are punctuated by a narrow Cottrellian-type region attributed to a monophasic domain (~50 mA h/g). In comparison, the minimally present bell shapes during subsequent Li-ion (de)insertion processes (green line) due to a Cottrellian-type current decay indicate a primarily topotactic reaction mechanism. In contrast, *m*-FSH exhibits two deep bell-shaped curves in each (dis)charge cycle. Indeed, on lithiation, the pristine monoclinic framework of *m*-FSH (s.g. $C2/c$) transforms into a triclinic framework (s.g. $P\bar{1}$).[18] Overall, *o*-FSH exhibits a phase change during the first discharge followed by a dominant solid solution redox mechanism accompanied by likely minor structural changes as opposed to *m*-FSH undergoing a biphasic reaction in all cycles. The Fe^{3+}/Fe^{2+} redox potential is nearly identical in each polymorph: *o*-FSH (3.15 V) and *m*-FSH (3.2 V) vs Li^+/Li. It was also noted that the electronic structure calculations revealed Fe^{3+}/Fe^{2+} as redox-active ions in LiFSH Supporting Information

The phase evolution during (de)lithiation of *o*-FSH was probed by synergizing operando and ex-situ XRD techniques (see Figure 7). A thin sheet of *o*-FSH composite was used as the positive electrode in an in-house-developed operando cell with an X-ray transparent Be window on the cathodic side. The cell was electrochemically cycled at a current rate of C/35 (Figure S7), while the XRD patterns were recorded continuously (operando) with an acquisition time of 10 min (see Figure 7a). The characteristic XRD peaks of *o*-FSH: (002), (201), and (020), disappear at about 50% of the first Li insertion process. In addition, two new peaks grow at 24.3 and 27.2° and disappear before reaching 2 V, whereas another peak appears at 26.3°. Evidently, the first discharge of *o*-FSH proceeds through a structural change. In the following (dis)charge segments, a gradual shift in the XRD peaks is observed, attributed to a monophasic Li reaction mechanism.

https://doi.org/10.1021/acs.chemmater.4c01652
Chem. Mater. 2024, 36, 8088−8097

However, the operando XRD analysis is still qualitative due to the higher noise-to-intensity ratio of the diffractograms. Therefore, this is complemented by an ex-situ XRD study. In this case, measurements on the Swagelok-type cells were stopped at different states of charge and cycles, and the respective X-ray diffractograms were compared (Figure 7b). The polytetrafluoroethylene (PTFE) has a characteristic peak at 18.1°, as seen for the pristine electrode sheet. The higher intensity of the (020) peak compared to the (201) peak, unlike the *o*-FSH and C mixture, is due to the rolling process during electrode fabrication. As noted, a new XRD pattern is observed at 2 V with a significant background contribution arising likely from an amorphous phase in the lithiated Li_xFSH product. In addition, the XRD pattern resembles the tavorite-type $LiFeSO_4F$[38] and $LiFeSO_4OH$ (s.g. $P\bar{1}$).[16−18] The end product may be a mixture of crystalline and amorphous phases. On subsequent Li ion extraction, the pristine *o*-FSH phase is reclaimed (Figure 7b). The background contribution increases as the signal-to-noise ratio decreases at 2 V in the 2nd and 25th cycles while maintaining the structural reversibility to the pristine phase (Figure 7b). Once again, the deviation of the Li (de)insertion mechanism of *o*-FSH from *m*-FSH is underlined.[18]

The amorphization of the pristine phase during lithiation has also been reported for hydroxy-based polyanionic compounds $NaFe_3(SO_4)_2(OH)_6$ and tavorite $LiFePO_4OH$, and it is reflected as an upshift in the galvanostatic discharge profile in the second cycle.[24,39] While in the case of $LiFePO_4OH$, a completely irreversible structural breakdown occurs, the layered $NaFe_3(SO_4)_2(OH)_6$ follows an amorphous−crystalline transformation based on a solid solution mechanism due to the reversible breakage of Fe−O−S bonds creating strongly corrugated nonperiodic layers in the amorphous phase (inorganic polymer-like phase). Figure 7 The possible occurrence of a minor amount of an amorphous phase during cell cycling warrants further investigation using synchrotron diffraction.

3. CONCLUSIONS

We have successfully demonstrated orthorhombic $FeSO_4OH$ as a novel low-cost ∼3.2 V polyanionic insertion host for Li-ion batteries with a reversible capacity of ∼100 mA h/g (C/20). This environmentally benign hydroxysulfate cathode is synthesized using a facile hydrothermal route at 190 °C for 5 h. The particle morphology exposes the (020) plane, which is also favorable for fast electrode kinetics. This hydroxysulfate framework provides fast two-dimensional Li ion migration pathways with a low activation energy barrier (0.26 eV). The orthorhombic $FeSO_4OH$ polymorph undergoes a partial structural transformation during the first cycle, resulting in the reversible formation of an amorphous matrix and crystalline Li_xFeSO_4OH phase linked to the labile Fe−O−S bonds. The sloped (dis)charge profile may stem from the combined effect of amorphization and the differently oriented SO_4 units within the crystalline *o*-FSH framework. Overall, this study not only enriches the database of Fe-based cathode materials but also stimulates further exploration of earth-abundant and low-cost polyanionic insertion hosts for Li-ion batteries.

4. EXPERIMENTAL METHODS

4.1. Synthesis. Orthorhombic $FeSO_4OH$ was prepared by using a hydrothermal route. The precursor $Fe_2(SO_4)_3{\cdot}xH_2O$ (Sigma-Aldrich, 75% assay) was dissolved in deionized water, resulting in the formation of a translucent brown-colored solution. Subsequently, this solution was transferred and filled up to 75% of a 25 mL Teflon-lined hydrothermal reactor, which was heated to 190 °C (heating rate = 5 °C/min) for 5 h. Post furnace cooling, the product was repeatedly rinsed with water and was recuperated by centrifugation. Finally, the material was rinsed with ethanol, centrifuged, and dried in a hot air oven at 70 °C for 12 h. The target compound has an off-yellow color. The influence of synthesis conditions on the structure and morphology of the final product phase was examined by varying the annealing temperature (140−200 °C) and duration (5−60 h). Monoclinic $FeSO_4OH$ was synthesized by the heat treatment of $FeSO_4{\cdot}7H_2O$ at 280 °C for 1 week in air.

4.2. Structural Characterization. The powder X-ray diffraction (PXRD) patterns were acquired using a PANalytical Empyrean X-ray diffractometer (PANanalytical, Malvern, UK) having a Cu Kα source (λ_1 = 1.5405 Å, λ_2 = 1.5443 Å) operating at 40 kV/30 mA. PXRD patterns were collected in Bragg−Brentano geometry (reflection mode) in the 2θ range of 10−80° with a step size of 0.026°. Rietveld analysis was performed with the ED-PCR program embedded in the FullProf suite.[40] Crystal structures were illustrated using VESTA software.[41]

The total X-ray scattering data for PDF analysis was carried out using a Rigaku SmartLab X-ray diffractometer (Mo rotating anode, no monochromator, λ = 0.711465 Å, HyPix3000 detector) in transmission mode for the sample contained in 0.6 mm quartz capillary using Si as standard. The PDFgetX[42] and PDFgui[43] programs were used to extract and analyze experimental PDF.

The powder morphology was observed using a Carl Zeiss Ultra55 field emission scanning electron microscope, equipped with a thermal field emission-type tungsten source operating at 0.1−30 kV.

4.3. Electrochemical Characterization. The pristine powder and carbon (70:20) were hand mixed for 30 min by using a mortar and pestle. The final active material/Super P carbon/PTFE binder ratio was maintained at 70/20/10 with the appropriate addition of PTFE binder into the powder mixture. Rolled electrode sheets were then obtained, which served as the working electrodes. For powder cell, the pristine powder was intimately milled with Super P carbon (80:20) using Spex 8000 M miller for 40 min with a protocol of 4 × 10 min with 10 min intermittent rest. The Swagelok-type half cells and CR-2032-type coin cells were assembled inside an Ar-filled glovebox (MBraun GmbH, 3 mbar, O_2 and H_2O < 0.5 ppm) with the following configuration: cathode | glass fiber separator soaked with 1 M $LiClO_4$ dissolved in PC acting as electrolyte | Li metal foil (as counter and reference electrode). These cells were electrochemically cycled by using BioLogic BCS-805/810 workstations. The galvanostatic titration technique was performed at a current rate of C/80 with a (dis)charge step of 1 h with intermittent 1 h rest. The potentiostatic titration technique was performed at a potential step of 5 mV for 1 h with current decay set to $|i| \leq C/100$.

4.4. Operando and Ex-Situ XRD Characterization. For ex-situ XRD, the Swagelok-type cells were disconnected at different voltages (or states of charge) of the galvanostatic cycle. Subsequently, the cells were dissembled inside the glovebox. The recovered cathode was washed with anhydrous dimethyl carbonate and later dried before further characterizations. As hydroxysulfate-based materials have been observed to be air/moisture resistant, ex-situ XRDs were acquired without any protection.

The operando XRD measurements were carried out during electrochemical cycling to monitor the underlying structural modification. The study was carried out using an X-ray transparent electrochemical cell (Swagelok type) with Be window on the cathodic side.[44] A Rigaku MiniFlex600 diffractometer, equipped with a high-speed one-dimensional D/teX Ultra2 detector and a Cu rotating anode working at 40 kV and 15 mA, was used to acquire operando XRD data. The diffractograms were acquired in the 2θ range of 10−50° at the step of 0.01° with an overall acquisition time of 10 min.

4.5. Computational Methods. As the methods used for the atomistic simulation and DFT studies are well established,[35,37] general outlines of the employed methods are given here. Force-field-based

https://doi.org/10.1021/acs.chemmater.4c01652
Chem. Mater. 2024, 36, 8088−8097

simulations were carried out to examine intrinsic defects, which have been applied to a range of polyanion cathodes including $LiFePO_4$, Li_2FeSiO_4, and $Li_2Fe(SO_4)_2$.[37,45,46] The long-range electrostatic and short-range Buckingham potentials along with three body Morse potentials for SO_4 units were used for the atomistic simulations and are listed in Table S3 in Supporting Information. The lattice relaxation around the defects was performed using Mott−Littleton methods as implemented in the general utility lattice program code.[47,48] The advantage of using this method is that it considers thousands of ions in both regions, which is a challenging task for computation using electronic structure methods.

DFT studies were performed using a plane wave-based Vienna ab initio simulation package (VASP).[49−51] For structural modeling, a high cutoff value of 850 eV was chosen for the plane-wave basis sets with a *k*-points mesh density of at least 0.27/Å and the use of projector augmented wave potentials[52] and a revised Perdew−Burke−Ernzerhof for solids (PBEsol) functional.[1,53] Complete spin polarization was employed in the calculations, and the antiferromagnetic ordering of the spins of Fe atoms was found to be favorable. To treat the strongly correlated Fe-3*d* states, DFT + *U* correction was considered in the calculations using an effective *U* value of 4 eV.[37] To find the unknown Li positions in lithiated o-$LiFeSO_4OH$, AIMD simulations were performed in VASP with an *NVT* ensemble. The AIMD calculations were started with an optimized cell parameter for the lithiated o-$LiFeSO_4OH$ structure generated from o-FSH. The Nose−Hoover thermostat and the Verlet algorithm were used, with a 0.5 fs time step for 5 ps simulations to capture the rapid motion of light elements such as Li and H. To reduce the computational cost, a lower cutoff of plane-wave basis sets of 520 eV was chosen for the AIMD simulations and surface slab calculations. The activation barrier heights for Li-ions migration were calculated using the nudged elastic band (NEB) method and constrained energy minimization. Five images for the diffusion species were generated along each diffusion path at equal distances using the interpolation method, and the intermediatory images were optimized using the climbing image NEB algorithm within the VASP code.[54]

The SEs were calculated using the following formula

$$\mathrm{SE} = \frac{E_{\mathrm{surface}} - n \cdot E_{\mathrm{bulk}} - \sum_i m_i \cdot \mu_i}{2 \cdot A} \tag{3}$$

where E_{surface} and E_{bulk} are the total energies of the surface planes and bulk-$LiFeSO_4OH$, respectively, (using DFT), n is the number of formula units present in the surface plane, and A is the area of the surface plane. $\sum_i m_i\mu_i$ appears if the surface slab is nonstoichiometric, and $m_i\mu_i$ are the number of an element and the chemical potential of that element, respectively.

The cell voltages were calculated using a well-established methodology and based here on the following formula.

$$V = -\frac{E\{\mathrm{LiFeSO_4OH}\} - E\{Li_x\mathrm{FeSO_4OH}\} - (1-x) \times \mu\{\mathrm{Li}\}}{(1-x)} \tag{4}$$

where $E\{Y\}$ is the total energy for composition Y, x is the number of Li (de)inserted, and μ is the chemical potential of a single Li atom. Such DFT-based methods have been applied to a range of Li-ion cathodes.[35,55,56]

■ ASSOCIATED CONTENT

Supporting Information

Supporting Information is available free of charge at the ACS publication Web site. The Supporting Information is available free of charge at https://pubs.acs.org/doi/10.1021/acs.chemmater.4c01652.

Analysis of electronic structure and crystallographic data of o-Li_xFeSO_4OH, calculated surface free energy , interatomic potential, thermal stability of hydroxysulfates, BVSE calculations of diffusion barriers, GITT profile of o-Li_xFeSO_4OH, and galvanostatic voltage profiles of hydroxysulfates (PDF)

■ AUTHOR INFORMATION

Corresponding Authors

M. Saiful Islam − *Department of Materials, University of Oxford, Oxford OX1 3PH, U.K.;* orcid.org/0000-0003-3882-0285; Email: Saiful.islam@materials.ox.ac.uk

Prabeer Barpanda − *Faraday Materials Laboratory (FaMaL), Materials Research Center, Indian Institute of Science, Bangalore 560012, India; Helmholtz Institute Ulm (HIU), Ulm 89081, Germany; Institute of Nanotechnology, Karlsruhe Institute of Technology (KIT), Karlsruhe 76021, Germany;* orcid.org/0000-0003-0902-3690; Email: prabeer@iisc.ac.in

Authors

Shashwat Singh − *Faraday Materials Laboratory (FaMaL), Materials Research Center, Indian Institute of Science, Bangalore 560012, India; Normandie University, Caen 14000, France*

Arup Chakraborty − *Department of Materials, University of Oxford, Oxford OX1 3PH, U.K.*

Audric Neveu − *Normandie University, Caen 14000, France*

Pawan Kumar Jha − *Faraday Materials Laboratory (FaMaL), Materials Research Center, Indian Institute of Science, Bangalore 560012, India*

Valérie Pralong − *Normandie University, Caen 14000, France*

Maximilian Fichtner − *Helmholtz Institute Ulm (HIU), Ulm 89081, Germany; Institute of Nanotechnology, Karlsruhe Institute of Technology (KIT), Karlsruhe 76021, Germany;* orcid.org/0000-0002-7127-1823

Complete contact information is available at: https://pubs.acs.org/10.1021/acs.chemmater.4c01652

Author Contributions

S.S.: conceptualization, data curation, formal analysis, investigation, methodology, and writing−original draft; A.C.: DFT calculations, formal analysis, and writing−original draft; A.N.: data curation; P.K.J.: formal analysis and methodology; V.P.: supervision and writing−review and editing; M.F.: supervision and writing−review and editing; M.S.I.: supervision, funding acquisition, and writing−review and editing; P.B.: conceptualization, funding acquisition, project administration, supervision, and writing−review and editing.

Notes

The authors declare no competing financial interest.

■ ACKNOWLEDGMENTS

We acknowledge the financial support from the Technology Mission Division (Department of Science and Technology, Govt. of India) under the Materials for Energy Storage (MES-2018) program (DST/TMD/MES/2K18/207). S.S. and P.K.J. thank the Ministry of Human Resource Development (MHRD) for financial support. S.S., P.K.J., V.P., and P.B. are grateful to LAFICS (Indian-French Laboratory of Solid State Chemistry) for financial support. A.C. acknowledges the Royal Society Newton International Fellowship grant (NIF \R1\211700) for the funding. A.C. and M.S.I. thank the Faraday Institution CATMAT project (EP/S003053/1, FIRG016) for the Michael High-Performance Computing (HPC) facility (FIRG030). This work made use of the UK's

National Supercomputer, ARCHER2, through the HEC Materials Chemistry Consortium (EP/R029431). A.C. thanks Andrey Poletayev, Vikram, and Pezhman Zarabadi-Poor for fruitful discussions. P.B. is grateful to the Alexander von Humboldt Foundation (Bonn, Germany) for a 2022 Humboldt fellowship for experienced researchers.

REFERENCES

(1) Wu, F.; Maier, J.; Yu, Y. Guidelines and Trends for Next-generation Rechargeable Lithium and Lithium-ion Batteries. *Chem. Soc. Rev.* **2020**, *49* (5), 1569−1614.
(2) Zeng, X.; Li, M.; Abd El-Hady, D.; Alshitari, W.; Al-Bogami, A. S.; Lu, J.; Amine, K. Commercialization of Lithium Battery Technologies for Electric Vehicles. *Adv. Energy Mater.* **2019**, *9* (27), 1900161.
(3) Thackeray, M. M.; Johnson, C. S.; Vaughey, J. T.; LiCurrent address eVionyx Inc Ha, N.; Hackney, S. A. Advances in Manganese-Oxide "Composite" Electrodes for Lithium-Ion Batteries. *J. Mater. Chem.* **2005**, *15* (23), 2257.
(4) Clarke, F. W.; Washington, H. S. *The Composition of the Earth's Crust*; US Department of Interior: Washington DC, 1924.
(5) Padhi, A. K.; Manivannan, V.; Goodenough, J. B. Tuning the Position of the Redox Couples in Materials with NASICON Structure by Anionic Substitution. *J. Electrochem. Soc.* **1998**, *145* (5), 1518−1520.
(6) Padhi, A. K.; Nanjundaswamy, K. S.; Goodenough, J. B. Phospho-olivines as Positive-Electrode Materials for Rechargeable Lithium Batteries. *J. Electrochem. Soc.* **1997**, *144* (4), 1188−1194.
(7) Yamada, A.; Iwane, N.; Harada, Y.; Nishimura, S.; Koyama, Y.; Tanaka, I. Lithium Iron Borates as High-Capacity Battery Electrodes. *Adv. Mater.* **2010**, *22* (32), 3583−3587.
(8) Nytén, A.; Abouimrane, A.; Armand, M.; Gustafsson, T.; Thomas, J. O. Electrochemical Performance of Li_2FeSiO_4 as a New Li-Battery Cathode Material. *Electrochem. Commun.* **2005**, *7* (2), 156−160.
(9) Nishimura, S.; Nakamura, M.; Natsui, R.; Yamada, A. New Lithium Iron Pyrophosphate as 3.5 V Class Cathode Material for Lithium Ion Battery. *J. Am. Chem. Soc.* **2010**, *132* (39), 13596−13597.
(10) Barpanda, P.; Ati, M.; Melot, B. C.; Rousse, G.; Chotard, J.-N.; Doublet, M.-L.; Sougrati, M. T.; Corr, S. A.; Jumas, J.-C.; Tarascon, J.-M. A 3.90 V Iron-Based Fluorosulphate Material for Lithium-Ion Batteries Crystallizing in the Triplite Structure. *Nat. Mater.* **2011**, *10* (10), 772−779.
(11) Recham, N.; Chotard, J.-N.; Dupont, L.; Delacourt, C.; Walker, W.; Armand, M.; Tarascon, J.-M. A 3.6 V Lithium-Based Fluorosulphate Insertion Positive Electrode for Lithium-Ion Batteries. *Nat. Mater.* **2010**, *9* (1), 68−74.
(12) Ben Yahia, M.; Lemoigno, F.; Rousse, G.; Boucher, F.; Tarascon, J.-M.; Doublet, M.-L. Origin of the 3.6 to 3.9 V Voltage Increase in the $LiFeSO_4F$ Cathodes for Li-Ion Batteries. *Energy Environ. Sci.* **2012**, *5* (11), 9584.
(13) Zhang, L.; Tarascon, J.-M.; Sougrati, M. T.; Rousse, G.; Chen, G. Influence of Relative Humidity on the Structure and Electrochemical Performance of Sustainable $LiFeSO_4F$ Electrodes for Li-Ion Batteries. *J. Mater. Chem. A* **2015**, *3* (33), 16988−16997.
(14) Singh, S.; Lochab, S.; Sharma, L.; Pralong, V.; Barpanda, P. An Overview of Hydroxy-Based Polyanionic Cathode Insertion Materials for Metal-Ion Batteries. *Phys. Chem. Chem. Phys.* **2021**, *23* (34), 18283−18299.
(15) Swamy, M. S. R.; Prasad, T. P.; Sant, B. R. Thermal Analysis of Ferrous Sulphate Heptahydrate in Air: Part I. Some General Remarks and Methods. *J. Therm. Anal.* **1979**, *15* (2), 307−314.
(16) Anji Reddy, M.; Pralong, V.; Caignaert, V.; Varadaraju, U. V.; Raveau, B. Monoclinic Iron Hydroxy Sulphate: A New Route to Electrode Materials. *Electrochem. Commun.* **2009**, *11* (9), 1807−1810.
(17) Avdeev, M.; Singh, S.; Barpanda, P.; Ling, C. D. Crystal and Magnetic Structures of Monoclinic $FeOHSO_4$. *Inorg. Chem.* **2021**, *60* (20), 15128−15130.
(18) Ati, M.; Sougrati, M.-T.; Rousse, G.; Recham, N.; Doublet, M.-L.; Jumas, J.-C.; Tarascon, J.-M. Single-Step Synthesis of FeSO 4F1 yOH y($0 \leq y \leq 1$) Positive Electrodes for Li-Based Batteries. *Chem. Mater.* **2012**, *24* (8), 1472−1485.
(19) Eames, C.; Clark, J. M.; Rousse, G.; Tarascon, J.-M.; Islam, M. S. Lithium Migration Pathways and van Der Waals Effects in the $LiFeSO_4OH$ Battery Material. *Chem. Mater.* **2014**, *26* (12), 3672−3678.
(20) Manthiram, A.; Goodenough, J. B. Lithium Insertion into $Fe_2(SO_4)_3$Frameworks. *J. Power Sources* **1989**, *26* (3−4), 403−408.
(21) Subban, C. V.; Ati, M.; Rousse, G.; Abakumov, A. M.; Van Tendeloo, G.; Janot, R.; Tarascon, J.-M. Preparation, Structure, and Electrochemistry of Layered Polyanionic Hydroxysulfates: $LiMSO_4OH$ (M = Fe, Co, Mn) Electrodes for Li-Ion Batteries. *J. Am. Chem. Soc.* **2013**, *135* (9), 3653−3661.
(22) Johansson, G.; Yhland, M.; Dahlbom, R.; Sjövall, J.; Theander, O.; Flood, H. On the Crystal Structures of $FeOHSO_4$ and $InOHSO_4$. *Acta Chem. Scand.* **1962**, *16*, 1234−1244.
(23) Wills, A. S.; Harrison, A. Structure and Magnetism of Hydronium Jarosite, a Model Kagomé Antiferromagnet. *J. Chem. Soc., Faraday Trans.* **1996**, *92* (12), 2161−2166.
(24) Gnanavel, M.; Pralong, V.; Lebedev, O. I.; Caignaert, V.; Bazin, P.; Raveau, B. Lithium Intercalation into the Jarosite-Type Hydroxysulfate: A Topotactic Reversible Reaction from a Crystalline Phase to an Inorganic Polymer-like Structure. *Chem. Mater.* **2014**, *26* (15), 4521−4527.
(25) Ventruti, G. The Order-Disorder Character of $FeOHSO_4$ Obtained from the Thermal Decomposition of Metahohmannite, $Fe^{3+}_2(H_2O)_4[O(SO_4)_2]$. *Am. Mineral.* **2005**, *90* (4), 679−686.
(26) Aronsson, R.; Jansson, B.; Knape, H. E. G.; Lundén, A.; Nilsson, L.; Sjöblom, C. A.; Torell, L. M. Fast Ion Conductors with Rotating Sulphate Ions. *J. Phys. Colloq.* **1980**, *41* (C6), C6-35−C6-37.
(27) Majzlan, J.; Dachs, E.; Benisek, A.; Plášil, J.; Sejkora, J. Thermodynamics Crystal Chemistry and Structural Complexity of the $Fe(SO_4)(OH)(H_2O)_x$ Phases: $Fe(SO_4)(OH)$, Metahohmannite, Butlerite, Parabutlerite, Amarantite, Hohmannite, and Fibroferrite. *Eur. J. Mineral.* **2018**, *30* (2), 259−275.
(28) Ventruti, G.; Della Ventura, G.; Gomez, M. A.; Capitani, G.; Sbroscia, M.; Sodo, A. High-Temperature Study of Basic Ferric Sulfate, FeOHSO4. *Phys. Chem. Miner.* **2020**, *47* (10), 43.
(29) Chapman, K. W. Emerging *Operando* and X-Ray Pair Distribution Function Methods for Energy Materials Development. *MRS Bull.* **2016**, *41* (3), 231−240.
(30) Lander, L.; Reynaud, M.; Rousse, G.; Sougrati, M. T.; Laberty-Robert, C.; Messinger, R. J.; Deschamps, M.; Tarascon, J.-M. Synthesis and Electrochemical Performance of the Orthorhombic $Li_2Fe(SO_4)_2$ Polymorph for Li-Ion Batteries. *Chem. Mater.* **2014**, *26* (14), 4178−4189.
(31) Rahm, J.; Erhart, P. WulffPack: A Python Package for Wulff Constructions. *J. Open Source Softw.* **2020**, *5* (45), 1944.
(32) Islam, M. S.; Driscoll, D. J.; Fisher, C. A. J.; Slater, P. R. Atomic-Scale Investigation of Defects, Dopants, and Lithium Transport in the $LiFePO_4$ Olivine-Type Battery Material. *Chem. Mater.* **2005**, *17* (20), 5085−5092.
(33) Fisher, C. A. J.; Hart Prieto, V. M.; Islam, M. S. Lithium Battery Materials $LiMPO_4$ (M = Mn, Fe, Co, and Ni): Insights into Defect Association, Transport Mechanisms, and Doping Behavior. *Chem. Mater.* **2008**, *20* (18), 5907−5915.
(34) Brown, I. D. The Chemical Bond in Inorganic Chemistry: The Bond Valence Model. *International Union of Crystallography Book Series*, 2nd ed.; Oxford University Press: Oxford, 2016.
(35) Islam, M. S.; Fisher, C. A. J. Lithium and Sodium Battery Cathode Materials: Computational Insights into Voltage, Diffusion and Nanostructural Properties. *Chem. Soc. Rev.* **2014**, *43* (1), 185−204.
(36) *Computational Approaches to Energy Materials*; Catlow, R., Sokol, A., Walsh, A., Eds.; Wiley, 2013.
(37) Clark, J. M.; Eames, C.; Reynaud, M.; Rousse, G.; Chotard, J.-N.; Tarascon, J.-M.; Islam, M. S. High Voltage Sulphate Cathodes

https://doi.org/10.1021/acs.chemmater.4c01652
Chem. Mater. 2024, 36, 8088−8097

$Li_2M(SO_4)_2$ (M = Fe, Mn, Co): Atomic- Scale Studies of Lithium Diffusion, Surfaces and Voltage Trends. *J. Mater. Chem. A* **2014**, *2* (20), 7446−7453.
(38) Melot, B. C.; Rousse, G.; Chotard, J.-N.; Ati, M.; Rodríguez-Carvajal, J.; Kemei, M. C.; Tarascon, J.-M. Magnetic Structure and Properties of the Li-Ion Battery Materials $FeSO_4F$ and $LiFeSO_4F$. *Chem. Mater.* **2011**, *23* (11), 2922−2930.
(39) Ellis, B. L.; Ramesh, T. N.; Rowan-Weetaluktuk, W. N.; Ryan, D. H.; Nazar, L. F. Solvothermal Synthesis of Electroactive Lithium Iron Tavorites and Structure of Li_2FePO_4F. *J. Mater. Chem.* **2012**, *22* (11), 4759.
(40) Rodríguez-Carvajal, J. Recent Advances in Magnetic Structure Determination by Neutron Powder Diffraction. *Phys. B* **1993**, *192* (1−2), 55−69.
(41) Momma, K.; Izumi, F. *VESTA 3* for Three-Dimensional Visualization of Crystal, Volumetric and Morphology Data. *J. Appl. Crystallogr.* **2011**, *44* (6), 1272−1276.
(42) Juhás, P.; Davis, T.; Farrow, C. L.; Billinge, S. J. L. *PDFgetX3*: A Rapid and Highly Automatable Program for Processing Powder Diffraction Data into Total Scattering Pair Distribution Functions. *J. Appl. Crystallogr.* **2013**, *46* (2), 560−566.
(43) Farrow, C. L.; Juhas, P.; Liu, J. W.; Bryndin, D.; Božin, E. S.; Bloch, J.; Proffen, T.; Billinge, S. J. L. PDFfit2 and PDFgui: Computer Programs for Studying Nanostructure in Crystals. *J. Phys.: Condens. Matter* **2007**, *19* (33), 335219.
(44) Sottmann, J.; Pralong, V.; Barrier, N.; Martin, C. An Electrochemical Cell for *Operando* Bench-Top X-Ray Diffraction. *J. Appl. Crystallogr.* **2019**, *52* (2), 485−490.
(45) Armstrong, A. R.; Kuganathan, N.; Islam, M. S.; Bruce, P. G. Structure and Lithium Transport Pathways in Li_2FeSiO_4 Cathodes for Lithium Batteries. *J. Am. Chem. Soc.* **2011**, *133* (33), 13031−13035.
(46) Fisher, C. A. J.; Islam, M. S. Surface Structures and Crystal Morphologies of $LiFePO_4$: Relevance to Electrochemical Behaviour. *J. Mater. Chem.* **2008**, *18* (11), 1209.
(47) Gale, J. D. GULP: A Computer Program for the Symmetry-Adapted Simulation of Solids. *J. Chem. Soc., Faraday Trans.* **1997**, *93* (4), 629−637.
(48) Gale, J. D.; Rohl, A. L. The General Utility Lattice Program (GULP). *Mol. Simul.* **2003**, *29* (5), 291−341.
(49) Kresse, G.; Furthmüller, J. Efficiency of Ab-Initio Total Energy Calculations for Metals and Semiconductors Using a Plane-Wave Basis Set. *Comput. Mater. Sci.* **1996**, *6* (1), 15−50.
(50) Kresse, G.; Hafner, J. *Ab Initio* Molecular Dynamics for Liquid Metals. *Phys. Rev. B: Condens. Matter Mater. Phys.* **1993**, *47* (1), 558−561.
(51) Kresse, G.; Hafner, J. *Ab Initio* Molecular-Dynamics Simulation of the Liquid-Metal−Amorphous-Semiconductor Transition in Germanium. *Phys. Rev. B: Condens. Matter Mater. Phys.* **1994**, *49* (20), 14251−14269.
(52) Blöchl, P. E. Projector Augmented-Wave Method. *Phys. Rev. B: Condens. Matter Mater. Phys.* **1994**, *50* (24), 17953−17979.
(53) Perdew, J. P.; Ruzsinszky, A.; Csonka, G. I.; Vydrov, O. A.; Scuseria, G. E.; Constantin, L. A.; Zhou, X.; Burke, K. Erratum: Restoring the Density-Gradient Expansion for Exchange in Solids and Surfaces [Phys. Rev. Lett.**100**, 136406 (2008)]. *Phys. Rev. Lett.* **2009**, *102* (3), 039902.
(54) Henkelman, G.; Uberuaga, B. P.; Jónsson, H. A Climbing Image Nudged Elastic Band Method for Finding Saddle Points and Minimum Energy Paths. *J. Chem. Phys.* **2000**, *113* (22), 9901−9904.
(55) McColl, K.; House, R. A.; Rees, G. J.; Squires, A. G.; Coles, S. W.; Bruce, P. G.; Morgan, B. J.; Islam, M. S. Transition Metal Migration and O_2 Formation Underpin Voltage Hysteresis in Oxygen-Redox Disordered Rocksalt Cathodes. *Nat. Commun.* **2022**, *13*, 5275.
(56) Sharpe, R.; House, R. A.; Clarke, M. J.; Förstermann, D.; Marie, J.-J.; Cibin, G.; Zhou, K.-J.; Playford, H. Y.; Bruce, P. G.; Islam, M. S. Redox Chemistry and the Role of Trapped Molecular O_2 in Li-Rich Disordered Rocksalt Oxyfluoride Cathodes. *J. Am. Chem. Soc.* **2020**, *142* (52), 21799−21809.

https://doi.org/10.1021/acs.chemmater.4c01652
Chem. Mater. 2024, 36, 8088−8097